

## Strong and tough magnesium-MAX phase composites with nacre-like lamellar and brick-and-mortar architectures

Yanyan Liu<sup>1,2,5</sup>, Xi Xie<sup>2,5</sup>, Zengqian Liu<sup>1,2</sup>, Qin Yu<sup>3</sup>, Xuegang Wang<sup>2</sup>, Shaogang Wang<sup>2</sup>, Qing Jia<sup>1,2</sup>, Zhefeng Zhang<sup>1,2</sup>, Rui Yang<sup>2,4</sup> & Robert O. Ritchie<sup>3</sup>

Bioinspired nacre-like structures are effective in toughening materials, yet are difficult to construct in magnesium-ceramic systems. Here, a set of magnesium-MAX phase composites with nacre-like lamellar and brick-and-mortar architectures are fabricated by pressureless infiltration of the magnesium melt into ice-templated  $Ti_3AlC_2$  ceramic scaffolds. The structure and mechanical properties of the composites are elucidated with a special focus on the effects of the types of architectures (lamellar or brick-and-mortar) and matrices (pure magnesium or AZ91D alloy) on the toughening mechanisms. The nacre-like architectures are found to play a role in blunting the cracks via plastic deformation and microcracking, and shielding the cracks from applied stress by promoting crack deflection and uncracked-ligament bridging mechanisms. These composites achieve a good combination of specific strength and fracture toughness, which are superior to many other reported magnesium-ceramic and nacre-like metal-ceramic composite materials.

<sup>1</sup>School of Materials Science and Engineering, University of Science and Technology of China, Shenyang 110016, China. <sup>2</sup>Institute of Metal Research, Chinese Academy of Sciences, Shenyang 110016, China. <sup>3</sup>Department of Materials Science and Engineering, University of California Berkeley, Berkeley, CA 94720, USA. <sup>4</sup>Center for Adaptive System Engineering, School of Creativity and Art, ShanghaiTech University, Shanghai 201210, China. <sup>5</sup>These authors contributed equally: Yanyan Liu, Xi Xie. ✉email: [zengqianliu@imr.ac.cn](mailto:zengqianliu@imr.ac.cn); [zhfzhang@imr.ac.cn](mailto:zhfzhang@imr.ac.cn); [yangrui@shanghaitech.edu.cn](mailto:yangrui@shanghaitech.edu.cn)

Magnesium (Mg) and Mg alloys are promising for weight-critical structural applications owing to their low density, high specific stiffness and specific strength, i.e., stiffness and strength normalized by density, and good damping capacity<sup>1</sup>. However, when compared to other common structural metals, e.g., steels and aluminum alloys, Mg and Mg alloys are inferior in their stiffness and strength in terms of the absolute values at ambient to elevated temperatures; moreover, they exhibit relatively low fracture toughness at room temperature. A feasible approach to strengthening Mg and Mg alloys is through the introduction of a reinforcement phase into the Mg matrix, in particular by making Mg-ceramic composites<sup>2–4</sup>. In this regard, the MAX phase ceramics appear to be an ideal choice. These ceramics, having the general formula of  $M_{n+1}AX_n$  (M: early transition metal; A: group A element; X: C and/or N;  $n = 1–3$ ), are a family of ternary carbides or nitrides with mixed metallic-covalent-ionic atomic bonds. Their characteristics are essentially a combination of the property advantages from both metals, e.g., good thermal/electrical conductivity and thermal shock resistance, and ceramics, e.g., high hardness and stiffness, high strength at ambient to elevated temperatures and high corrosion resistance<sup>5–8</sup> also, they display a good damage tolerance owing to their layered atomic structure<sup>9</sup>. Moreover, the MAX phase ceramics of Ti–Al–C system have been shown to exhibit good wettability with Mg to form strong interfacial bonding<sup>10–12</sup>. They therefore represent an attractive reinforcement phase for Mg and Mg alloys.

There are reports in the literature on the fabrication of such Mg-MAX phase composites to achieve high mechanical strength and good damping properties<sup>10–14</sup>. Nevertheless, despite the lack of data on their fracture toughness, these composites, especially those with relatively high ceramic content exceeding 20 vol.%, were found to fracture in a brittle manner without undergoing visible plastic deformation<sup>12–14</sup>. Indeed, it is a general compromise for metal-ceramic composites that the strength is improved at a cost of fracture toughness<sup>15</sup>. In the case of Mg-ceramic composites (in bulk form), their fracture toughness normally cannot even reach 10 MPa  $m^{0.5}$  when the specific flexural strength exceeds 150 MPa ( $g\ cm^{-3}$ )<sup>-1</sup>; toughnesses above 10 MPa  $m^{0.5}$  have only been attained in lower-strength composites<sup>16–18</sup>.

Natural nacre, which features a layered structure comprising ~95 vol.% aragonite platelets with ~5 vol.% organic matter, exhibits much more superior combination of strength and fracture toughness than its constituents<sup>19, 20</sup>. Taking the inspiration from nacre offers an effective approach for developing new high-performance composite materials<sup>21–23</sup>. The so-called lamellar and brick-and-mortar architectures are two of the most common structural arrangements mimicking nacre<sup>21,24–29</sup>. The stiff and soft constituents are alternately arranged in a layered fashion for the former; whereas the stiff platelets (bricks) are more closely stacked and staggered between each other at adjacent layers within the soft matrix (mortar) for the latter. These two architectures also show a large difference in their phase constitution, i.e., the stiff constituent accounts for a larger volume fraction in the brick-and-mortar architecture than in the lamellar one.

Nature-inspired nacre-like architectures have been constructed in a variety of composite materials, including those of ceramic-polymer<sup>21,24,25</sup>, metal-ceramic<sup>26,27</sup>, and metal-graphene systems<sup>30,31</sup>. Such architectural designs have been proven to be effective in activating a series of toughening mechanisms<sup>21–28,30</sup>, such as crack deflection, uncracked-ligament bridging and frictional sliding between crack faces, thereby playing an effective role in toughening materials. In particular, the ice templating technique, based on the assembly of particles in the slurry driven by the growth of ice crystals<sup>32,33</sup>, offers a viable means for fabricating porous scaffolds with preferentially aligned structures.

Nacre-like lamellar architectures can be constructed by infiltrating a second phase into the ice-templated porous scaffolds, whereas the densification of the scaffolds before infiltration results in nacre-like brick-and-mortar architectures<sup>21</sup>. A series of nacre-like composites have been developed in different combinations of metal-ceramic systems using such methods<sup>17,26,27,32</sup>. However, it is not easy to construct nacre-like architectures, especially the brick-and-mortar architectures, in Mg-based composites. This is largely due to that the Mg melt exhibits a high reactivity and tends to react at high temperatures with many of the possible reinforcement phases to form brittle intermetallics, or otherwise displays a poor wettability with them<sup>3,34</sup>. On the other hand, the mechanical properties of nacre-like composites are closely associated with the type of architectures and the characteristics of matrices<sup>21,25,26</sup> nevertheless, these factors and their effects remain to be explored for Mg-based composites.

Here, nacre-like lamellar and brick-and-mortar architectures were constructed in a set of bioinspired Mg-MAX phase composites by pressureless infiltration of the melt of pure Mg or AZ91D alloy into ice-templated  $Ti_3AlC_2$  porous scaffolds. The mechanical properties of the resultant composites are investigated and correlated to the types of their architectures (lamellar or brick-and-mortar) and matrices (pure Mg or AZ91D alloy). The nacre-like architectures play a role in toughening the composites by promoting crack bifurcation and blunting and inducing crack-tip shielding, thereby endow the composites with high fracture toughness in addition to high specific strength.

## Results

**Composite formation.** Nacre-like architectures were constructed by employing the ice templating technique. As illustrated in Supplementary Fig. 1, during the freezing process of slurry, the  $Ti_3AlC_2$  platelets and additives contained in the slurry were gradually expelled by the growing ice crystals into their inter-spaces, and as such were assembled into an ordered lamellar architecture. The subsequent sublimation of ice led to the formation of well-aligned pores as the replica of ice crystals in the bulk. Porous  $Ti_3AlC_2$  scaffolds with lamellar architecture were then obtained by sintering the freeze-dried samples. In order to construct the brick-and-mortar architecture, the sintered scaffolds were densified by uniaxially pressing along the normal direction of ceramic lamellae to break the lamellae into small fragments (bricks) that were closely stacked. The densified scaffolds were then re-sintered to form interconnections between adjacent bricks at their contacts. As shown in the Supplementary Fig. 2, the bricks were closely stacked, staggered between adjacent layers, and interconnected through overlapping or via bridges. Finally, nacre-like Mg-MAX phase composites with lamellar and brick-and-mortar architectures were obtained by infiltrating the metal melt respectively into the ice-templated and densified scaffolds. In this process, the spatial arrangement of ceramic phase was retained into the infiltrated composites. The  $Ti_3AlC_2$  powders were delaminated into ultrafine platelets by controlled ball-milling before ice templating procedure. This helped refine the structure of resultant composites to generate a high strengthening efficiency. It also acted to reduce the relatively weak interlayers in the MAX phase, which is beneficial for avoiding the easy delamination of ceramic phase in the composites.

**Microstructural characteristics.** Figure 1 shows the microstructures and chemical characteristics of the infiltrated Mg-MAX phase composites. The metal and ceramic-rich constituents showed an alternate arrangement in a layered fashion in the composites (Fig. 1a, b). The frequency distributions of the thicknesses of metal and ceramic-rich constituent layers in the

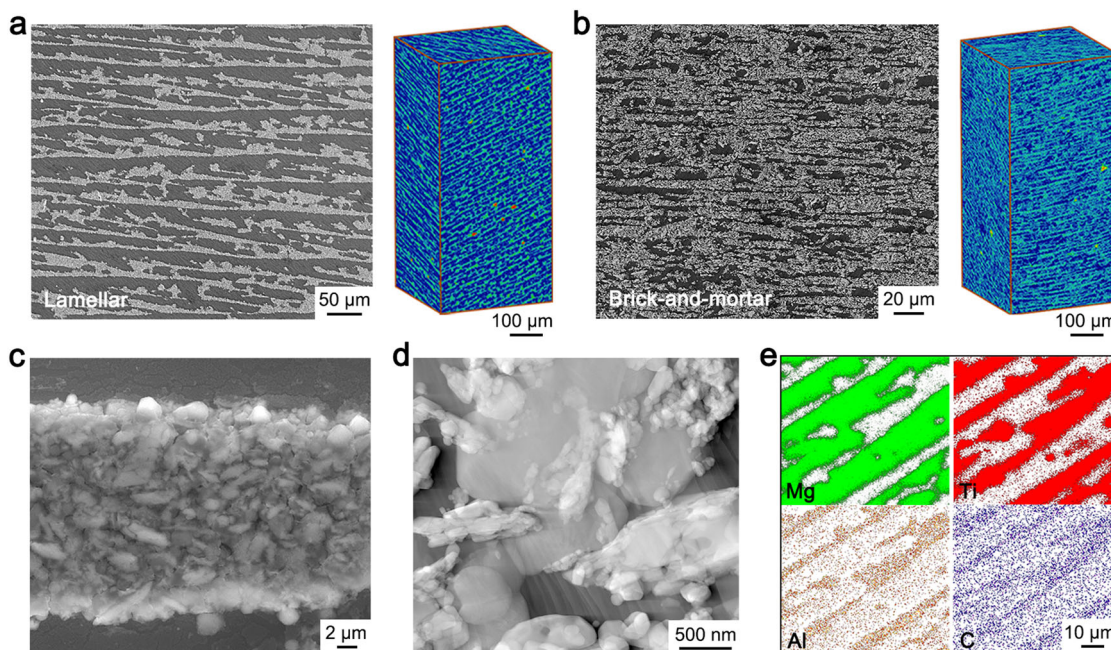


**Fig. 1** Microstructures and chemical characteristics of the nacre-like Mg-MAX phase composites. SEM micrographs and XRT volume renderings of the Mg-MAX phase composites with nacre-like lamellar (a) and brick-and-mortar (b) architectures. Magnified SEM (c) and STEM (d) micrographs of the ceramic-rich constituent in the composites showing its ultrafine composite structure (c: pure Mg composite with lamellar architecture; d: AZ91D alloy composite with brick-and-mortar architecture). e Distribution of elements measured by EDS in the AZ91D alloy composite with lamellar architecture.

composites are shown in Supplementary Fig. 3. The ceramic-rich constituents were interconnected in three-dimensional (3D) space between layers, via bridges for the lamellar architecture and by overlapping for the brick-and-mortar one. Both architectures were qualitatively similar with that of natural nacre, specifically in terms of the alternating arrangement of relatively soft and hard constituents in a layered fashion and the interconnection between layers. Specifically for the brick-and-mortar architecture, the ceramic-rich constituents were more closely stacked (i.e., with smaller thickness of metal layer), staggered between layers, and accounted for a larger volume fraction in the composites as compared to the lamellar one. Such architecture has been widely referred to as the “brick-and-mortar” architecture to distinguish it from the lamellar one<sup>21,25,26</sup>. In both architectures, the ceramic-rich constituents were indeed composed of both metal and ceramic phases (Fig. 1c), instead of monolithic ceramics, showing an ultrafine composite structure where the metal phase filled the interspaces between ceramic platelets (Fig. 1d). This is different from the common case in other nacre-like metal-ceramic composites made by ice templating technique where constituents are mixed only at one specific length scale. The grain size of metal phase within the layer was typically smaller than 1 μm (Fig. 1d). Such structure was formed because of the filling of metal melt into the layer during melt infiltration and the constraint of ceramic phase on the growth of metal grains during the subsequent solidification process.

The volume fractions of pores were determined by X-ray tomography (XRT) imaging to be  $\sim 2.5 \times 10^{-4}$  vol.% and  $\sim 8.5 \times 10^{-3}$  vol.%, respectively, in the composites with lamellar and brick-and-mortar architectures (Supplementary Fig. 4). Such tiny porosities indicated an almost complete filling of the ceramic scaffolds with metal during the melt infiltration process. By neglecting the pores, the respective volume fractions of ceramic and metal phases in the composites,  $V_{\text{cer}}$  and  $V_{\text{met}}$ , can be assessed based on the measured densities of composites using the Archimedes method,  $\rho$ , according to  $\rho = \rho_{\text{cer}} V_{\text{cer}} + \rho_{\text{met}} V_{\text{met}}$  with

$V_{\text{cer}} + V_{\text{met}} = 1$ .  $\rho_{\text{cer}}$  is the density of the  $\text{Ti}_3\text{AlC}_2$  MAX phase as  $4.21 \text{ g cm}^{-3}$ , and  $\rho_{\text{met}}$  denotes the density of the metal phase which is  $1.74 \text{ g cm}^{-3}$  and  $1.82 \text{ g cm}^{-3}$  for pure Mg and AZ91D alloy, respectively. For the composites with pure Mg and AZ91D alloy as the metal component,  $V_{\text{cer}}$  was calculated to be  $\sim 11.3$  vol.% and  $\sim 14.0$  vol.% for the lamellar architecture, and  $\sim 32.6$  vol.% and  $\sim 32.5$  vol.% for the brick-and-mortar architecture, respectively. The volume fractions of the metal and ceramic-rich constituent layers in the composites,  $V_{\text{met}}^{\text{L}}$  and  $V_{\text{cer}}^{\text{L}}$ , can be determined by image analysis (with  $V_{\text{met}}^{\text{L}} + V_{\text{cer}}^{\text{L}} = 1$ ). Then, the volume fractions of the metal and ceramic phases within the ceramic-rich constituents,  $V_{\text{met}}^{\text{cer}}$  and  $V_{\text{cer}}^{\text{cer}}$ , can be obtained according to  $V_{\text{cer}}^{\text{cer}} = V_{\text{cer}} / V_{\text{cer}}^{\text{L}}$  and  $V_{\text{met}}^{\text{cer}} = 1 - V_{\text{cer}}^{\text{cer}}$ , respectively. By such means,  $V_{\text{met}}^{\text{cer}}$  was derived to be  $\sim 63.5\%$  and  $\sim 54.1\%$  for the pure Mg and AZ91D alloy composites with the lamellar architecture, and to be  $\sim 36.5\%$  and  $\sim 37.4\%$  for those with the brick-and-mortar architecture, respectively. The detailed phase constitutions of the nacre-like composites are presented in Supplementary Table 1.

Energy dispersive X-ray spectroscopy (EDS) analysis revealed that the Mg element and the elemental Ti, Al and C were principally concentrated in the metal and ceramic-rich constituents (Fig. 1e and Supplementary Fig. 5), respectively. This, combined with the X-ray diffraction (XRD) results (Supplementary Fig. 6), clearly indicated that the composites largely retained the pre-designed phase constitution of Mg and  $\text{Ti}_3\text{AlC}_2$  phases after melt infiltration. In addition, a small amount of MgO and  $\text{Mg}_{17}\text{Al}_{12}$  phases were also recognized in the XRD patterns. They should be the product of the interfacial reaction between the Mg melt and the  $\text{Ti}_3\text{AlC}_2$  phase (along with its surface oxides) during the melt infiltration process. As shown in Supplementary Fig. 7, oxides, which were identified mainly as  $\text{Al}_2\text{O}_3$  and  $\text{TiO}_2$  and can react with molten Mg to form  $\text{MgO}$ <sup>35, 36</sup>, were formed on the surfaces of ball-milled  $\text{Ti}_3\text{AlC}_2$  platelets (the oxygen content in the platelets was measured to be  $\sim 4.2$  wt.%). It has been established that the interfacial reactions between ceramic and metal phases generally

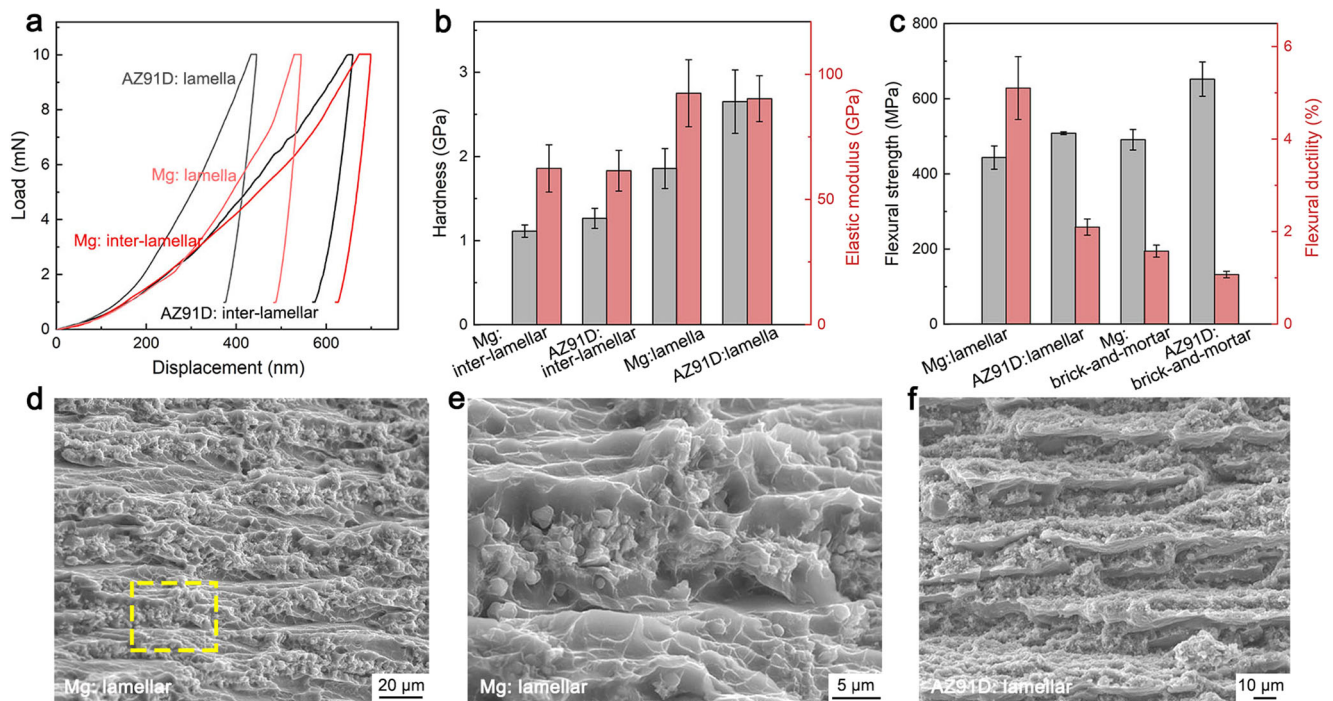


**Fig. 2 Mechanical properties of the nacre-like Mg-MAX phase composites.** Representative load-displacement curves (a) and the hardness and elastic modulus (b) measured by nanoindentation testing for the metal (inter-lamellar) and ceramic-rich (lamella) constituents in the pure Mg and AZ91D alloy composites with lamellar architecture. c Flexural strength and ductility of the Mg-MAX phase composites with different architectures and metal components. SEM micrographs of the fracture surfaces for the pure Mg (d, e) and AZ91D alloy (f) composites with lamellar architecture after bending. e is a magnified view of the yellow dashed box in d. Error bars represent standard deviation from the mean.

play a role in promoting their wettability, thereby facilitating the infiltration. For metal (such as Mg and Ag)-MAX phase systems, interfacial reactions have been revealed to improve the interfacial bonding strength between ceramic and metal phases<sup>37–39</sup>. A strong interface is beneficial for enhancing the strength of composites and ensuring the toughening effect of bioinspired architectures by avoiding easy interfacial cracking.

**Mechanical properties.** The nacre-like Mg-MAX phase composites exhibited large differences in their local mechanical properties. As shown in Fig. 2a, for the lamellar architecture subject to an equal load under nanoindentation condition, relatively larger displacements were obtained: (i) in the metal constituent (inter-lamellar region) than in the ceramic-rich constituent (lamella) for the same type of metal component, or (ii) in the composites with pure Mg than AZ91D alloy than in the metal component for the same regions. The local mechanical properties measured by nanoindentation testing are presented in Supplementary Table 2. Specifically, the nanoindentation hardness of the ceramic-rich constituents was markedly higher than that of the inter-lamellar region respectively by  $\sim 1.7$  and  $\sim 2.1$  times in the pure Mg and AZ91D alloy composites (Fig. 2b). Additionally, the lamella and inter-lamellar regions of the AZ91D alloy composites were harder by  $\sim 1.4$  and  $\sim 1.1$  times, respectively, than in the pure Mg composites. However, the local elastic moduli were similar between the composites containing the two types of metal components, both measured to be  $\sim 91.4$  GPa and  $\sim 61.9$  GPa, respectively, for the lamella and inter-lamellar regions.

The global mechanical properties of the composites were also related to the types of nacre-like architectures and metal components. For the same type of metal component, the brick-and-mortar architecture with larger volume fraction of MAX phase exhibited higher flexural strengths than the lamellar one, respectively up to  $491.1 \pm 27.4$  MPa and  $652.4 \pm 45.9$  MPa for the

pure Mg and AZ91D alloy composites (Fig. 2c and Supplementary Fig. 8). Nevertheless, this was accompanied by an obvious compromise in the ductility for both metal components. With respect to the effects of metal component, the AZ91D alloy composites invariably displayed relatively higher flexural strengths when considering the same type of architecture, whereas the pure Mg composites displayed better ductility. Such trend is qualitatively consistent with that for their metal components (Supplementary Fig. 9). All these composites showed microscopically staircase-like morphologies on their fracture surfaces, which conformed to their layered structure (Fig. 2d–f). No obvious pores were discerned on the fracture surfaces of the composites, implicating that the tiny pores may not severely deteriorate their mechanical properties. Apparent dimples that are indicative of plastic deformation were formed in the metal constituent for the pure Mg composites with lamellar architecture (Fig. 2d, e). Such feature became much less evident in the AZ91D alloy composites (Fig. 2f), consistent with their reduced ductility.

**Fracture toughness.** Under single-edge notched bending conditions, instantaneous fracture occurred at the maximum bending load without stable crack propagation in the AZ91D alloy composites with brick-and-mortar architecture, as shown in Supplementary Fig. 8. In comparison, the bending load decreased with increasing displacement after reaching its maximum in the other composites. In particular, the pure Mg composites with the lamellar architecture showed gradual load drop along with a large displacement, indicating a stable cracking process. The fracture resistance of the composites in terms of  $J$ -integral and equivalent stress intensity  $K_I$  as a function of crack extension ( $\Delta a$ ) are shown in Fig. 3a, b. The AZ91D alloy composites with brick-and-mortar architecture fractured abruptly at the onset of crack propagation, giving  $J$  and  $K$  of  $2.1 \pm 0.7$  kJ m<sup>-2</sup> and

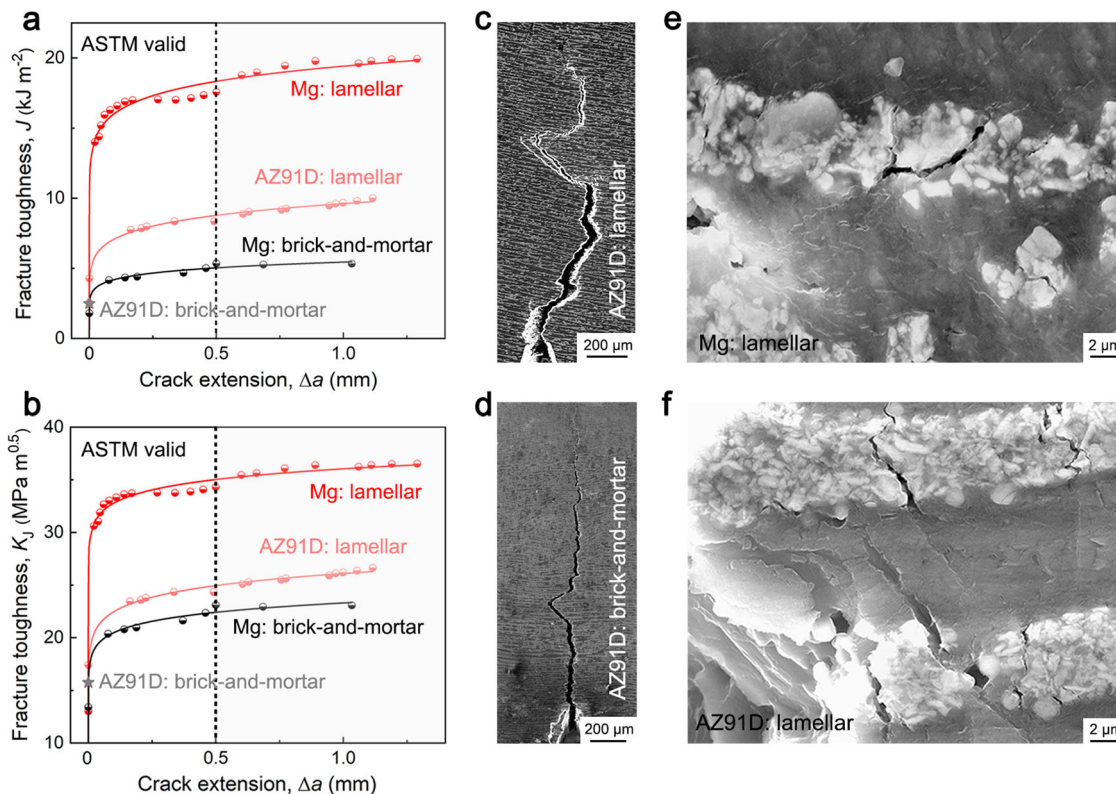


**Fig. 3** Fracture toughness of the nacre-like Mg-MAX phase composites. Variation in the  $J$ -integral (a) and equivalent  $K$ -based fracture resistance  $K_J$  (b) as a function of the crack extension  $\Delta a$  for the composites. The solid curves were obtained by data fitting according to the ASTM Standard E1820<sup>40</sup>. SEM micrographs showing the cracking paths in the composites with lamellar (c) and brick-and-mortar (d) architectures (by taking the AZ91D alloy composites as examples). SEM micrographs showing the damage characteristics near the primary cracks in pure Mg (e) and AZ91D alloy (f) composites with lamellar architecture.

$14.4 \pm 2.7 \text{ MPa m}^{0.5}$ , respectively. However, all the other composites, i.e., the AZ91D alloy composites with lamellar architecture and the pure Mg composites, displayed a stable increase in  $J$  and  $K_J$  with crack extension, showing rising crack resistance-curve (R-curve) behavior. Higher fracture toughness was generated in the lamellar architecture for both types of metal components, or in the pure Mg composites for a given type of architecture. In particular, the pure Mg composites with lamellar architecture exhibited the highest fracture toughness, with the critical  $J$  and  $K_J$  up to respectively  $15.9 \pm 2.5 \text{ kJ m}^{-2}$  and  $32.5 \pm 2.6 \text{ MPa m}^{0.5}$ , which were determined by the maximum crack extension of  $\sim 0.5 \text{ mm}$  according to the ASTM Standard E1820<sup>40</sup> (as indicated by the dashed lines).

The nacre-like architectures have been proven to be effective in activating a series of extrinsic toughening mechanisms for toughening materials, such as crack deflection, uncracked-ligament bridging and frictional sliding between crack faces<sup>15, 21</sup>. These mechanisms were clearly introduced into the Mg-MAX phase composites by the lamellar architecture, as manifested by the obviously tortuous cracking paths (Fig. 3c and Supplementary Fig. 10); nevertheless, such behavior became much less evident for the brick-and-mortar architecture (Fig. 3d). With regard to the effects of the type of metal component, obvious plastic deformation occurred in the inter-lamellar region near the primary crack in the pure Mg composites with lamellar architecture; whereas microcracks were formed in the ceramic-rich constituents (Fig. 3e). In comparison, for the AZ91D alloy composites, both lamella and inter-lamellar regions exhibited apparent microcracking without visible plastic deformation (Fig. 3f).

## Discussion

Both plastic deformation and microcracking in the vicinity of the crack tip, which are dominant respectively in pure Mg and AZ91D alloy composites, offer a means for dissipating mechanical energy and can promote crack bifurcation. These mechanisms, which can be termed intrinsic toughening mechanisms<sup>15,41</sup>, are principally active ahead of the crack tip to blunt the crack tip. In addition, they play a role in promoting the crack deflection following the slip bands in inter-lamellar regions or along the microcracks and inducing the formation of uncracked-ligament bridges, i.e., between the main cracks and voids or microcracks. These mechanisms, which can be termed extrinsic toughening mechanisms<sup>15,41</sup>, are principally active at or behind the crack tip to reduce the crack-driving force actually experienced at the crack tip, thereby shielding the crack tip from applied stress.

The effectiveness of the above toughening mechanisms in the nacre-like Mg-MAX phase composites is associated with the types of architectures (lamellar or brick-and-mortar) and metal components (pure Mg or AZ91D alloy). The composites with brick-and-mortar architecture contain much larger volume fraction of ceramic phase compared to the lamellar one, and exhibit higher strength but lower ductility. However, the lamellar architecture, which features a larger volume fraction of metal phase than the brick-and-mortar one, enables a more stable crack extension via crack deflection, bifurcation and uncracked-ligament bridging mechanisms, leading to higher crack-growth toughness after the onset of cracking. Such trend is opposite to that found in nacre-like composites of ceramic-polymer (polymethylmethacrylate or epoxy resin)<sup>21,25</sup> and alumina-metallic glass<sup>26</sup> systems where the brick-and-mortar architecture is tougher than the lamellar one.

The interfaces between hard and soft constituents play an important role in toughening the bioinspired nacre-like composites. Crack deflection tends to occur along relatively weak interfaces or soft phases, and additionally induces the formation of uncracked-ligament bridges behind the crack tip. These extrinsic toughening mechanisms are particularly effective in the brick-and-mortar architecture owing to its higher density of interfaces and bridges than in the lamellar one. They act as the main sources of fracture resistance in the composites where the soft phases (polymethylmethacrylate, epoxy resin, or metallic glass) are brittle and can hardly undergo large plastic deformation.

For the current Mg-MAX phase composites, the relatively hard phase (i.e., ceramic-rich constituent) is composed of both ceramic and metal phases, rather than merely ceramics. The metal phase exhibits relatively good plastic deformability and demonstrates a strong interfacial bonding with the ceramic phase. Obvious plastic deformation occurs in the metal layer near the primary crack in the pure Mg composites with lamellar architecture; whereas microcracks are formed in the ceramic-rich constituent probably preferentially at the interfaces between metal and ceramic phases within the constituent. In comparison, for the AZ91D alloy composites, both metal and ceramic-rich constituents exhibit apparent microcracking without visible plastic deformation. With respect to the effects of the metal component, pure Mg exhibits much lower strength but better ductility than the AZ91D alloy in the as-cast state, and thereby can be more easily deformed to blunt the cracks in the Mg-MAX phase composites. Such easy inelastic deformation of the soft phase, as compared to the fracture of stiff constituents, is essential for ensuring the toughening effects of the nacre-like architectures in promoting both the intrinsic and extrinsic mechanisms<sup>15,21</sup>. As such, for the same type of architecture (i.e., with similar volume fraction of ceramic phase), the pure Mg composites invariably exhibit higher ductility and fracture toughness but lower strength than the AZ91D alloy composites.

Figure 4a presents a comparison of the fracture toughness and flexural strength for the Mg-MAX phase composites with their component materials of pure Mg, AZ91 series alloys and bulk  $\text{Ti}_3\text{AlC}_2$  ceramics<sup>5,6,16,17,42–45</sup>. Most MAX phase ceramics were

reported to exhibit a flexural strength of less than 560 MPa (although they can be strengthened by fine modulation of their microstructures<sup>46</sup>). The fracture toughness for crack initiation ( $K_{\text{IC}}$ ) typically ranges from 4  $\text{MPa m}^{0.5}$  to 10  $\text{MPa m}^{0.5}$  for most of MAX phase ceramics, even though higher toughness may be obtained after some crack growth or by designing coarse-grained or textured structures<sup>7–9</sup>. Specifically with respect to the  $\text{Ti}_3\text{AlC}_2$  ceramics, the fracture toughness rarely exceeds 10  $\text{MPa m}^{0.5}$ <sup>55,6</sup>. Pure Mg and AZ91 series alloys generally exhibit a flexural strength below 400 MPa and a fracture toughness of lower than 22  $\text{MPa m}^{0.5}$ <sup>42–45</sup> (an exception exists for an AZ91 alloy after T4 treatment where the  $K_{\text{JC}}$  derived from  $J$  was reported to be around 30  $\text{MPa m}^{0.5}$ <sup>47</sup>). In comparison, the flexural strength of the nacre-like Mg-MAX phase composites is comparable to, or even higher than, those of monolithic  $\text{Ti}_3\text{AlC}_2$  ceramics, while their fracture toughness is comparable to that of the metal phase. This indicates the achievement of a good combination of property advantages in the composites from their constituent materials.

Figure 4b shows the variation in the flexural strength as a function of the ceramic content in Mg-based composites reinforced by different types of ceramics<sup>16, 17,43,44,48–50</sup>. The current Mg-MAX phase composites exhibit relatively higher flexural strength than most other materials at equal ceramic contents. Figure 4c shows a comparison of the specific fracture toughness and specific flexural strength, i.e., fracture toughness ( $K_{\text{IC}}$ ) and flexural strength normalized by density, for the nacre-like composites of different metal-ceramic systems fabricated by ice templating and subsequent melt infiltration procedures<sup>17,26,34,51–54</sup>. The current Mg-MAX phase composites show a high specific flexural strength ranging from  $\sim 200 \text{ MPa (g cm}^{-3}\text{)}^{-1}$  to over  $250 \text{ MPa (g cm}^{-3}\text{)}^{-1}$  combined with a high specific fracture toughness. In particular, owing to the relatively low densities, their specific fracture toughness exceeds those of most other nacre-like metal-ceramic composites with the same level of specific flexural strength, even though their fracture toughness and strength are not such superior considering the absolute values. It is worth noting that recently we have developed a Mg-MAX phase composite with high strength over 1 GPa by infiltrating a Mg alloy melt into  $\text{Ti}_3\text{AlC}_2$  scaffold where the platelets are preferentially aligned by vacuum filtration<sup>55</sup>.

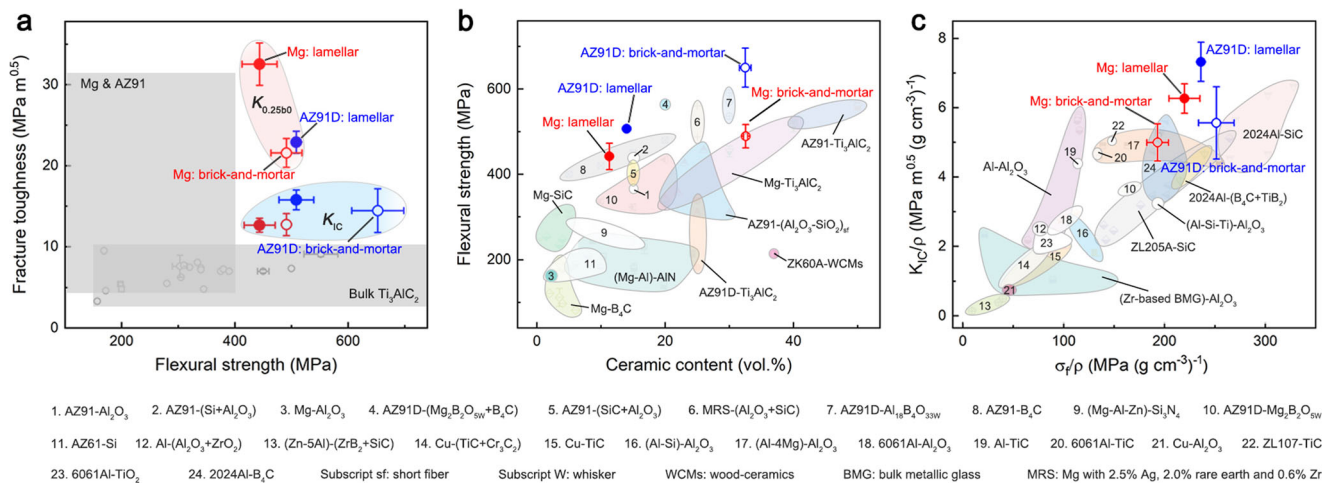


**Fig. 4 Comparison of mechanical properties for the nacre-like Mg-MAX phase composites with other materials.** **a** Fracture toughness versus flexural strength for the Mg-MAX phase composites and their component materials of bulk  $\text{Ti}_3\text{AlC}_2$  ceramics, pure Mg and AZ91 series alloys<sup>5,6,16,17,42–45</sup>.  $K_{0.25\text{mm}}$  denotes the critical  $K_{\text{J}}$  determined by the maximum crack extension of  $\sim 0.5 \text{ mm}$  according to the ASTM Standard E1820<sup>40</sup>. The toughness range for pure Mg and AZ91 alloys is defined using both  $K_{\text{IC}}$  and  $K_{\text{JC}}$  (which is derived from  $J$ ) values. **b** Variation in the flexural strength as a function of the ceramic content in the Mg and Mg alloy composites reinforced with different types of ceramic phases<sup>16,17,43,44,48–50</sup>. **c** Specific fracture toughness (in terms of  $K_{\text{IC}}$ ) versus specific flexural strength, i.e., normalized by density, for the nacre-like composites of different metal-ceramic systems fabricated by ice templating and subsequent melt infiltration procedures<sup>17,26,34,51–54</sup>. Error bars represent standard deviation from the mean.

Nevertheless, this composite tends to fracture catastrophically once cracks are initiated. In comparison, the current nacre-like Mg-MAX phase composites exhibit much higher damage tolerance at a moderate compromise of strength, and particularly demonstrate stable crack propagation featured by rising R-curve behavior. The good combination of properties makes these composites appealing for many lightweight structural applications.

## Conclusions

In summary, a set of Mg-MAX phase composites with nacre-like lamellar and brick-and-mortar architectures were fabricated by pressureless infiltration of pure Mg and AZ91D alloy melt into ice-templated porous  $\text{Ti}_3\text{AlC}_2$  scaffolds. The ceramic-rich constituents had an ultrafine structure comprising both ceramic and metal phases, were alternately arranged with metals in a layered fashion and interconnected between adjacent layers, but were more densely stacked in the brick-and-mortar architecture than in the lamellar one. The mechanical properties of the composites were associated with the types of architectures and metal components. Specifically, higher flexural strength, yet accompanied with inferior ductility, was generated in the AZ91D (Mg-Al-Zn-Mn) magnesium alloy composites for a given architecture or in the brick-and-mortar architecture for a given metal component. Apart from the AZ91D alloy composites with brick-and-mortar architecture, the Mg-MAX phase composites displayed rising R-curve behavior with stable crack propagation process. Crack advance involved bifurcation with crack blunting via plastic deformation and microcracking, which were respectively dominant in pure Mg and AZ91D alloy composites. Additionally, these materials were extrinsically toughened by crack deflection and uncracked-ligament bridging, resulting in significant crack-tip shielding – these mechanisms were more evident in the lamellar than in the brick-and-mortar architectures. The composites achieved an effective combination of the property advantages from their component materials. They were stronger than most other Mg-ceramic composites at equal ceramic contents and exhibited a good combination of specific fracture toughness and specific flexural strength among nacre-like metal-ceramic composites, thereby demonstrating a potential for lightweight structural applications. We believe that this study may further give insights for the design of new high-performance Mg-based composites.

## Methods

**Preparation of ultrafine  $\text{Ti}_3\text{AlC}_2$  platelets.** Commercial  $\text{Ti}_3\text{AlC}_2$  powders (400 mesh, Haixin metal, China) were ball milled in an ethanol dispersant in a mixed gas of 20 vol.% oxygen and 80 vol.% argon at a speed of 500 rpm for 48 h. The MAX phase ceramics display a relatively weak bonding between MX and A layers. During the ball milling process, shearing and delamination tend to occur along the MX/A interfaces, leading to the separation of  $\text{Ti}_3\text{AlC}_2$  powders into ultrafine platelets<sup>56,57</sup>, as shown in Supplementary Fig. 11. Oxygen-containing environment was employed as the newly formed surfaces of powders can be stabilized by forming surface oxides via oxidation reactions, thereby promoting the delamination process.

The ball-milled powders were examined by X-ray diffraction (XRD) using a powder diffractometer (Rigaku Smartlab, Japan) and X-ray photoelectron spectroscopy (XPS) analysis using ESCALAB Xi+ (Thermo Fisher Scientific, USA) with Al-K $\alpha$  radiation and a pass energy of 50 eV. The XRD results revealed that the platelets mainly consisted of  $\text{Ti}_3\text{AlC}_2$  phase with the oxides almost indiscernible because of their small amount (Supplementary Fig. 7). The XPS results revealed that oxides, which were identified mainly as  $\text{Al}_2\text{O}_3$  and  $\text{TiO}_2$ , were formed on the surfaces of MAX phase. The oxygen contents in the platelets as well as in the raw  $\text{Ti}_3\text{AlC}_2$  powders were measured using a TCH-600 N/H/O analyzer (LECO, USA). The equivalent particle size of the platelets was measured to be 100–300 nm using laser diffraction granulometry with a Mastersizer 2000 laser diffractometer (Malvern Instrument, UK) equipped with a Hydro 2000MU accessory (Malvern Instrument, UK).

**Fabrication of Mg-MAX phase composites.** The platelets were dried in air for 2 days and then were dispersed in deionized water at a mass ratio of 1:2 (i.e., giving a volume fraction of MAX phase as ~10.6%) under ultrasonic treatment at 50 W for 0.5 h. The slurry was mixed with an ammonium polymethacrylate anionic dispersant (Darvan CN, R.T. Vanderbilt, USA), polyvinyl alcohol (Meryer, China) and hydroxypropyl methylcellulose (Meryer, China), which accounted, respectively, for 0.2 wt.%, 1.5 wt.% and 0.5 wt.% of the platelets. These additives were used for promoting dispersion, increasing the viscosity of slurry to mitigate gravitational sedimentation, and binding the platelets after the removal of water.

The slurry was ball milled at a speed of 25 rpm for 24 h, and then was poured into a cuboid Teflon mold with an inner square cross-section of 30 mm  $\times$  30 mm which was fixed onto a customized freezing apparatus. The mold was designed to have non-uniform lateral walls which was thinner at one side (3 mm) than the other three sides (20 mm), and was sealed using a wedge with a slope angle of 25° at its bottom with the thinner end of the wedge conforming to the thinner wall of the mold. Such designs were implemented to create a horizontal temperature gradient in addition to the vertical one in the slurry during the freezing process<sup>58,59</sup>. The mold was descended at a constant rate of 0.6 mm min<sup>-1</sup> to immerse into an insulated box containing liquid nitrogen until the slurry was fully frozen. The frozen body was demolded and freeze-dried in a vacuum below 5 Pa for at least 72 h using a Scientz-10ND freeze drier (Scientz Biotechnology, China). Porous  $\text{Ti}_3\text{AlC}_2$  scaffolds with lamellar architecture were obtained by sintering the freeze-dried samples in flowing argon gas at 900 °C for 1 h. Some of the scaffolds were infiltrated with paraffin wax and then uniaxially pressed along the normal direction of lamellae at 75 °C (~15 °C higher than the melting point of paraffin wax) under a pressure of 20–35 MPa for 2 h for densification. These scaffolds were re-sintered in flowing argon gas at 950 °C for 1 h to create interconnections between adjacent lamellae or bricks.

Pure Mg with a purity of 99.99 wt.% and a widely used AZ91D cast Mg alloy (with ~8.5–9.5 wt.% Al, ~0.45–0.9 wt.% Zn and ~0.17–0.5 wt.% Mn) were used for fabricating the Mg-MAX phase composites. The sintered  $\text{Ti}_3\text{AlC}_2$  scaffolds were infiltrated with the melt of pure Mg or AZ91D alloy in flowing argon gas at 850 °C, some 250 °C higher than their melting points, for 1.5 h.

**Microstructural characterization.** The densities of the infiltrated composites were measured using the Archimedes' method<sup>60</sup>. The phase constitution was determined by XRD using a Bruker D8 Advance X-ray diffractometer (Bruker AXS, Germany) with Cu-K $\alpha$  radiation. Scanning electron microscopy (SEM) imaging was conducted using an Inspect F50 field-emission scanning electron microscope (FEI, USA) operating at an accelerating voltage of 20 kV. The SEM images were analyzed using the Image-Pro Plus software (Media Cybernetics, USA). Images with a total area over  $1.5 \times 10^5 \mu\text{m}^2$  were analyzed for each group of composites. Energy dispersive X-ray spectroscopy (EDS) measurements were carried out using a Bruker EDS system attached to the microscope. Scanning transmission electron microscopy (STEM) imaging was performed using a Tecnai-G2 F30 transmission electron microscope (FEI, USA) operating at an accelerating voltage of 300 kV. X-ray tomography (XRT) imaging was performed using an Xradia Versa XRM-500 3D X-ray microscope (Xradia, USA) operating at an accelerating voltage of 80 kV. A total of 1600 slices of 2D projections were acquired and then reconstructed to 3D volume renderings based on the Fourier back-projection algorithm. The spatial resolution of the obtained XRT images was ~0.96  $\mu\text{m}$  per pixel.

**Mechanical tests.** Nanoindentation tests were performed using a G200 nano indenter (KLA, USA) with a Berkovich diamond tip at a constant loading rate of 0.67 mN s<sup>-1</sup> to a peak load of 10 mN with a holding time of 10 s followed by unloading. The size of indent, which can be approximated based on the maximum indentation displacements in light of the geometrical characteristics of the Berkovich indenter, was smaller than the thickness of most of the metal and ceramic-rich layers in the composites with lamellar architecture. By selecting relatively thick layers for indentation, the indents can be completely located within the layers, as verified by the SEM images of one indent after unloading shown in Supplementary Fig. 12. Three-point bending tests were conducted using an Instron E1000 testing system (Instron, USA) at room temperature with a constant displacement rate of 0.1 mm min<sup>-1</sup> on beam samples with dimensions of 2 mm  $\times$  1.5 mm  $\times$  25 mm and a loading span of 20 mm, in line with the ASTM Standard C1161<sup>61</sup>. Single-edge notched bending tests were performed on a JEOL MicroTest stage inside the chamber of a JEOL JSM-6510 scanning electron microscope (JEOL, Japan) at a displacement rate of 5  $\mu\text{m}$  min<sup>-1</sup>. Samples with a width of 4 mm, thickness of 2 mm and loading span of 16 mm were side notched to ~2 mm in depth using a low-speed diamond wire saw with the notch sharpened to a tip radius of 5–10  $\mu\text{m}$  using a razor blade with 1  $\mu\text{m}$  diamond paste, in general accordance with the ASTM Standard E1820<sup>40</sup>. The loads in both three-point and single-edge notched bending tests were perpendicular to the layered structure of the composites, which is consistent with the general loading configuration for natural nacre. The fracture morphologies of samples were characterized by SEM imaging.

Nonlinear-elastic fracture mechanics methods were used to evaluate the fracture toughness of the composites in terms of their *J*-integral. The *J* values were calculated from the applied load and instantaneous crack length by considering the elastic ( $J_{el}$ ) and plastic ( $J_{pl}$ ) components, i.e.,  $J = J_{el} + J_{pl}$ , according to the ASTM Standard E1820<sup>40</sup>.  $J_{el}$  was formulated using the linear-elastic stress intensity factor

$K$  according to  $J_{el} = \frac{K^2(1-\nu^2)}{E}$ , where  $E$  is the Young's modulus and  $\nu$  is the Poisson's ratio. The elastic constants of the composites were assessed using those of the constituent phases based on their volume fractions. The  $E$  values were approximated using the averages of those calculated following the rule-of-mixtures under the iso-strain (Voigt model) and iso-stress (Reuss model) conditions<sup>62</sup>. In the case of single-edge notched bending tests, the mode I stress was principally parallel to the preferential alignment of nacre-like architectures, which is more similar with the iso-strain (Voigt model) loading configuration. Therefore, such approach was expected to give a conservative approximation for the Young's modulus and therefore for the fracture toughness. The Poisson's ratio  $\nu$  of the composites was approximated in a similar fashion to be 0.27 and 0.22, respectively, for the lamellar and brick-and-mortar architectures. The plastic component  $J_{pl}$  was calculated from the plastic area ( $A_{pl}$ ) under the load-displacement curve according to  $J_{pl} = \frac{1.9A_{pl}b^{1/2}}{Bb^{3/2}}$ , where  $B$  is the thickness of sample and  $b$  is the length of the uncracked ligament. The equivalent  $K$ -based stress intensity was obtained from the  $J$ -integral based on the standard  $J$ - $K$  equivalence as  $K_I = \left(\frac{JE}{(1-\nu^2)}\right)^{0.5}$  in the case of mode I fracture<sup>40</sup>.

### Data availability

The data that support the findings of this study are available in figshare with <https://doi.org/10.6084/m9.figshare.22650007>, and are also available from the corresponding author, Prof. Zengqian Liu, at [zengqianliu@imr.ac.cn](mailto:zengqianliu@imr.ac.cn), upon reasonable request.

Received: 26 July 2022; Accepted: 28 April 2023;

Published online: 09 May 2023

### References

- Pollock, T. M. Weight loss with magnesium alloys. *Science* **328**, 986–987 (2010).
- Chen, L. Y. et al. Processing and properties of magnesium containing a dense uniform dispersion of nanoparticles. *Nature* **528**, 539–543 (2015).
- Nguyen, Q. B., Tun, K. S., Lim, C. Y. H., Wong, W. L. E. & Gupta, M. Influence of nano-alumina and submicron copper on mechanical properties of magnesium alloy AZ31. *Compos. Part B Eng.* **55**, 486–491 (2013).
- Wang, Y., Wang, H. Y., Xiu, K., Wang, H. Y. & Jiang, Q. C. Fabrication of TiB<sub>2</sub> particulate reinforced magnesium matrix composites by two-step processing method. *Mater. Lett.* **60**, 1533–1537 (2006).
- Barsoum, M. W. & Radovic, M. Elastic and mechanical properties of the MAX phase. *Annu. Rev. Mater. Res.* **41**, 195–227 (2011).
- Sun, Z. M. Progress in research and development on MAX phases: a family of layered ternary compounds. *Int. Mater. Rev.* **56**, 143–166 (2011).
- Radovic, M. & Barsoum, M. W. MAX phases: bridging the gap between metals and ceramics. *Am. Ceram. Soc. Bull.* **92**, 20–27 (2013).
- Gonzalez-Julian, J. Processing of MAX phase: from synthesis to applications. *J. Am. Ceram. Soc.* **104**, 659–690 (2021).
- Gilbert, C. J. et al. Fatigue-crack growth and fracture properties of coarse and fine-grained Ti<sub>3</sub>SiC<sub>2</sub>. *Scr. Mater.* **42**, 761–767 (2000).
- Hu, W. Q. et al. Layered ternary MAX phases and their MX particulate derivative reinforced metal matrix composite: a review. *J. Alloys Compd.* **856**, 157313 (2021).
- Anasori, B., Caspi, E. N. & Barsoum, M. W. Fabrication and mechanical properties of pressureless melt infiltrated magnesium alloy composites reinforced with TiC and Ti<sub>2</sub>AlC particles. *Mater. Sci. Eng. A* **618**, 511–522 (2014).
- Yu, W. B. et al. Effects of A-site atoms in Ti<sub>2</sub>AlC and Ti<sub>3</sub>SiC<sub>2</sub> MAX phases reinforced Mg composites: interfacial structure and mechanical properties. *Mater. Sci. Eng. A* **826**, 141961 (2021).
- Kontsos, A. et al. Nanocrystalline Mg-MAX composites: mechanical behavior characterization via acoustic emission monitoring. *Acta Mater.* **59**, 5716–5727 (2011).
- Yu, W. B. et al. Microstructure, mechanical properties and fracture mechanism of Ti<sub>2</sub>AlC reinforced AZ91D composites fabricated by stir casting. *J. Alloys Compd.* **702**, 199–208 (2017).
- Ritchie, R. O. The conflicts between strength and toughness. *Nat. Mater.* **10**, 817–822 (2011).
- Luo, X. et al. Heterogeneous magnesium matrix nanocomposites with high bending strength and fracture toughness. *J. Alloys Compd.* **855**, 157359 (2021).
- Mao, H. R., Shen, P., Liu, Y. H., Zhao, Y. G. & Jiang, Q. C. Nacre-inspired lightweight and high-strength AZ91D/Mg<sub>2</sub>B<sub>2</sub>O<sub>5</sub>w composites prepared by ice templating and pressureless infiltration. *J. Mater. Sci.* **53**, 12167–12177 (2018).
- Lee, S., Sohn, K. S., Park, I. M. & Cho, K. M. Effect of applied pressure on mechanical properties of squeeze cast Mg matrix composites. *Met. Mater.* **1**, 37–46 (1995).
- Barthelat, F., Tang, H., Zavattieri, P. D., Li, C. M. & Espinosa, H. D. On the mechanics of mother-of-pearl: a key feature in the materials hierarchical structure. *J. Mech. Phys. Solids* **55**, 306–377 (2007).
- Loh, H. C. et al. Nacre toughening due to cooperative plastic deformation of stacks of co-oriented aragonite platelets. *Commun. Mater.* **1**, 77 (2020).
- Munch, E. et al. Tough, bio-inspired hybrid materials. *Science* **322**, 1516–1520 (2008).
- Bouville, F. et al. Strong, tough and stiff bioinspired ceramics from brittle constituents. *Nat. Mater.* **13**, 508–514 (2014).
- Zhao, H. W. & Guo, L. Nacre-inspired structural composites: performance-enhancement strategy and perspective. *Adv. Mater.* **29**, 1702903 (2017).
- Grossman, M. et al. Mineral nano-interconnectivity stiffens and toughens nacre-like composite materials. *Adv. Mater.* **29**, 1605039 (2017).
- Tan, G. Q. et al. Natural-inspired nacre-like composites combining human tooth-matching elasticity and hardness with exceptional damage tolerance. *Adv. Mater.* **31**, 1904603 (2019).
- Wat, A. et al. Bioinspired nacre-like alumina with a bulk-metallic glass-forming alloy as a compliant phase. *Nat. Commun.* **10**, 961 (2019).
- Ferraro, C. et al. Strong and tough metal/ceramic micro-laminates. *Acta Mater.* **144**, 202–215 (2018).
- Zhang, M. Y. et al. On the damage tolerance of 3-D printed Mg-Ti interpenetrating-phase composites with bioinspired architectures. *Nat. Commun.* **13**, 3247 (2022).
- Morsali, S., Qian, D. & Minary-Jolandan, M. Designing bioinspired brick-and-mortar composites using machine learning and statistical learning. *Commun. Mater.* **1**, 12 (2022).
- Xiong, D. B. et al. Graphene-and-copper artificial nacre fabricated by a preform impregnation process: bioinspired strategy for strengthening-toughening of metal matrix composite. *ACS Nano* **9**, 6934–6943 (2015).
- Zhang, X., Zhao, N. Q. & He, C. N. The superior mechanical and physical properties of nanocarbon reinforced bulk composites achieved by architecture design – a review. *Prog. Mater. Sci.* **113**, 100672 (2020).
- Launey, M. E. et al. A novel biomimetic approach to the design of high-performance ceramic-metal composites. *J. R. Soc. Interface* **7**, 741–753 (2010).
- Cheng, Q. F., Huang, C. J. & Tomsia, A. P. Freeze casting for assembling bioinspired structural materials. *Adv. Mater.* **29**, 1703155 (2017).
- Yao, Y. T. & Chen, L. Q. Processing of B<sub>4</sub>C particulate-reinforced magnesium-matrix composites by metal-assisted melt infiltration technique. *J. Mater. Sci. Technol.* **30**, 661–665 (2014).
- Liu, J. L., Suryanarayana, C., Ghosh, D., Subhash, G. & An, L. N. Synthesis of Mg-Al<sub>2</sub>O<sub>3</sub> nanocomposites by mechanical alloying. *J. Alloys Compd.* **563**, 165–170 (2013).
- Mounib, M., Pavese, M., Badini, C., Lefebvre, W. & Dieringa, H. Reactivity and microstructure of Al<sub>2</sub>O<sub>3</sub>-reinforced magnesium-matrix composites. *Adv. Mater. Sci. Eng.* **2014**, 1–6 (2014).
- Ye, L. et al. Interface design of Ti<sub>3</sub>C<sub>2</sub>T<sub>x</sub>/ZK61 composites by thermal reduction. *Mater. Sci. Eng. A* **831**, 142142 (2022).
- Ding, K. K. et al. Effect of Al atomic layer on the wetting behavior, interface structure and electrical contact properties of silver reinforced by Ti<sub>3</sub>AlC<sub>2</sub> ceramic. *Ceram. Int.* **48**, 190–198 (2022).
- Wang, D. D. et al. Comparison of the interfacial reactions and properties between Ag/Ti<sub>3</sub>AlC<sub>2</sub> and Ag/Ti<sub>3</sub>SiC<sub>2</sub> electrical contact materials. *J. Alloys Compd.* **857**, 157588 (2021).
- ASTM E1820-13. *Standard test method for measurement of fracture toughness* (ASTM International, Philadelphia, 2013).
- Kruzic, J. J., Nalla, R. K., Kinney, J. H. & Ritchie, R. O. Crack blunting, crack bridging and resistance-curve fracture mechanics in dentin: effect of hydration. *Biomaterials* **24**, 5209–5221 (2003).
- Somekawa, H. & Mukai, T. Effect of grain refinement on fracture toughness in extruded pure magnesium. *Scr. Mater.* **53**, 1059–1064 (2005).
- Pitchayyapillai, G. et al. Influence of B<sub>4</sub>C on mechanical properties of AZ91 magnesium matrix composites. *Mater. Today Proc.* **59**, 1438–1441 (2022).
- Park, I. M., Choi, L. D. & Cho, K. M. Mechanical and fracture behaviors of (Al<sub>2</sub>O<sub>3</sub>+SiC<sub>p</sub>)/AZ91 hybrid Mg matrix composite. *Mater. Sci. Forum.* **449**, 653–656 (2004).
- Ashby, M. Mapping the fracture properties of engineering materials. *Philos. Mag.* **93**, 3878–3892 (2013).
- Wang, W. J., Li, C. W., Zhai, H. X. & Wang, C. G. Preparation of high-strength Ti<sub>3</sub>AlC<sub>2</sub> by spark plasma sintering. *Appl. Ceram. Technol.* **12**, E126–E131 (2015).
- Kleiner, S., Beffort, O., Wahlen, A. & Uggowitz, P. J. Microstructure and mechanical properties of squeeze cast and semi-solid cast Mg-Al alloys. *J. Light Met.* **2**, 277–280 (2002).



48. Sohn, K. S., Euh, K., Lee, S. & Park, I. Mechanical property and fracture behavior of squeeze-cast Mg matrix composites. *Metall. Mater. Trans. A* **29**, 2543–2554 (1998).
49. Rangaraj, L., Sagar, R. V., Stalin, M., Raghavendra, K. & Venkateswarlu, K. Synthesis, characterization, and mechanical properties evaluation of Mg-Ti<sub>3</sub>AlC<sub>2</sub> composites produced by powder metallurgy/hot pressing. *Metall. Mater. Trans. A* **50**, 3714–3723 (2019).
50. Chen, J., Bao, C. G., Chen, W. H., Zhang, L. & Liu, J. L. Mechanical properties and fracture behavior of Mg-Al/AlN composites with different particle contents. *J. Mater. Sci. Technol.* **33**, 668–674 (2017).
51. Li, Y. L., Guo, R. F., Hu, Z. J. & Shen, P. Construction of nacre-mimetic composites with a “brick-and-mortar” architecture based on structural defects in ice-templating. *Mater. Des.* **204**, 109668 (2021).
52. Liu, Q. et al. Fabrication of a new SiC/2024Al co-continuous composite with lamellar microstructure and high mechanical properties. *J. Alloys. Compd.* **585**, 146–153 (2014).
53. Sun, M. Q., Shen, P. & Jiang, Q. C. Microstructures and mechanical characterizations of high-performance nacre-inspired Al/Al<sub>2</sub>O<sub>3</sub> composites. *Compos. Part A Appl. Sci. Manuf.* **121**, 465–473 (2019).
54. Wang, Y. et al. High damage-tolerance bio-inspired B<sub>4</sub>C/2024Al composites with adjustable mechanical performance by tuning ceramic thickness. *Mater. Sci. Eng. A* **819**, 141469 (2021).
55. Liu, Y. Y., et al. A strong, lightweight, and damping cermet material with a nacre-like ultrafine 3D interpenetrated architecture. *Mater. Today* **62**, 62–70 (2023).
56. Li, X. Q., Xie, X., Julian, J. G., Malzbender, J. & Yang, R. Mechanical and oxidation behavior of textured Ti<sub>2</sub>AlC and Ti<sub>3</sub>AlC<sub>2</sub> MAX phase materials. *J. Eur. Ceram. Soc.* **40**, 5258–5271 (2020).
57. Duan, X. M. et al. Synthesis of high-purity, isotropic or textured Cr<sub>2</sub>AlC bulk ceramics by spark plasma sintering of pressure-less sintered powders. *J. Eur. Ceram. Soc.* **35**, 1393–1400 (2015).
58. Bai, H. et al. Bioinspired hydroxyapatite/poly (methyl methacrylate) composite with a nacre-mimetic architecture by a bidirectional freezing method. *Adv. Mater.* **28**, 50–56 (2015).
59. Qiu, W. X. et al. Continuous ice-templating of macro-porous materials with uniformly ordered architecture. *Sci. China Mater.* **65**, 3134–3143 (2022).
60. Huguen, S. W. Archimedes revisited: a faster, better, cheaper method of accurately measuring the volume of small objects. *Phys. Educ.* **40**, 468–474 (2005).
61. ASTM C1161-18. *Standard test method for flexural strength of advanced ceramics at ambient temperature* (ASTM International, Philadelphia, 2018).
62. Watt, J. P., Davies, G. F. & O’Connell, R. J. The elastic properties of composite materials. *Rev. Geophys. Space Phys.* **14**, 541–563 (1976).

## Acknowledgements

The authors are grateful for the financial support by the National Key R&D Program of China (2020YFA0710404), the National Natural Science Foundation of China (52173269

and 51871216), the KC Wong Education Foundation (GJTD-2020-09), the Youth Innovation Promotion Association CAS, and the CAS Project for Young Scientists in Basic Research (YSBR-025). R.O.R. was supported by the Multi-University Research Initiative (AFOSR-FA9550-15-1-0009) from the Air Force Office of Scientific Research.

## Author contributions

Z.L. designed the research; Y.L. and X.X. fabricated the composites; Y.L. and S.W. characterized the microstructures; Y.L. and X.W. measured the mechanical properties; Y.L., Z.L., Q.Y., Q.J., Z.Z., R.Y. and R.O.R. analyzed and discussed the data; Y.L. and Z.L. wrote the initial paper; Z.Z., R.Y. and R.O.R. revised the paper.

## Competing interests

The authors declare no competing interests.

## Additional information

**Supplementary information** The online version contains supplementary material available at <https://doi.org/10.1038/s43246-023-00358-3>.

**Correspondence** and requests for materials should be addressed to Zengqian Liu, Zhifeng Zhang or Rui Yang.

**Peer review information** *Communications Materials* thanks Florian Bouville, Jinling Liu and the other, anonymous, reviewer(s) for their contribution to the peer review of this work. Primary Handling Editors: John Plummer. A peer review file is available

**Reprints and permission information** is available at <http://www.nature.com/reprints>

**Publisher’s note** Springer Nature remains neutral with regard to jurisdictional claims in published maps and institutional affiliations.



**Open Access** This article is licensed under a Creative Commons Attribution 4.0 International License, which permits use, sharing, adaptation, distribution and reproduction in any medium or format, as long as you give appropriate credit to the original author(s) and the source, provide a link to the Creative Commons license, and indicate if changes were made. The images or other third party material in this article are included in the article’s Creative Commons license, unless indicated otherwise in a credit line to the material. If material is not included in the article’s Creative Commons license and your intended use is not permitted by statutory regulation or exceeds the permitted use, you will need to obtain permission directly from the copyright holder. To view a copy of this license, visit <http://creativecommons.org/licenses/by/4.0/>.

© The Author(s) 2023